

Terahertz-optical mixing in undoped and doped GaAs quantum wells: From excitonic to electronic intersubband transitions

S. G. Carter,^{1,*} V. Ciulin,^{1,†} M. Hanson,² A. S. Huntington,^{2,‡} C. S. Wang,³ A. C. Gossard,^{2,3} L. A. Coldren,^{2,3} and M. S. Sherwin¹

¹*Physics Department and iQUEST, University of California, Santa Barbara, California 93106, USA*

²*Materials Department, University of California, Santa Barbara, California 93106, USA*

³*Electrical and Computer Engineering Department, University of California, Santa Barbara, California 93106, USA*

(Received 20 April 2005; revised manuscript received 30 June 2005; published 13 October 2005)

The mixing of near-infrared and terahertz (THz) beams has been observed in *n*-doped GaAs quantum wells (QWs) and is shown to be quite different from that in undoped QWs. The resonant behavior of the sidebands demonstrates that mixing in doped QWs is primarily sensitive to electronic intersubband transitions while that in undoped QWs is due to excitonic intersubband transitions. These results demonstrate that THz-optical mixing can be used to probe the collective dynamics of a driven electron gas.

DOI: [10.1103/PhysRevB.72.155309](https://doi.org/10.1103/PhysRevB.72.155309)

PACS number(s): 78.67.De, 42.65.-k, 73.21.Fg, 78.20.Jq

Nonlinear spectroscopy has become a powerful tool in studying a variety of different systems. In semiconductors, nonlinear techniques are routinely used to explore the dynamics of electrons.¹ These experiments provide far more information on the fundamental physics of semiconductors than linear spectroscopy alone and demonstrate methods of controlling optical processes. In this paper, nonlinear mixing of terahertz (THz) and near-infrared (NIR) radiation in doped GaAs quantum wells (QWs) is studied.

Previous experiments²⁻⁷ and theories^{8,9} have examined THz-optical mixing in undoped QWs. In these cases, excitonic interband resonances dominated the NIR spectra. The THz field did not drive a real intersubband (ISB) polarization as there were no free carriers. The mixing occurred as the THz field excited excitonic ISB transitions as part of a parametric process. The result of the mixing was that sidebands were generated at $\omega_{SB} = \omega_{NIR} + n\omega_{THz}$, where $n = \pm 1, 2, \dots$. The intensity of the sidebands was greatly enhanced when the NIR laser and/or sideband frequencies matched those of sharp (~ 1 meV wide) excitonic resonances. The $n = +1$ sidebands have been used to demonstrate the potential of THz-optical mixing for voltage-controlled, all-optical wavelength conversion.⁴⁻⁶ In strong THz fields, sidebands have been used to study nonperturbative effects induced by “dressing” the exciton states with the THz field.^{7,9}

One might expect THz-optical mixing to be weaker in doped quantum wells since excitons are screened, interband resonances are much broader, and some NIR transitions are Pauli blocked by the Fermi sea at low temperatures. However, in doped quantum wells, the THz radiation can excite an intersubband polarization directly, leading to a channel for sideband generation that has not been previously investigated. In this communication, THz-optical mixing is shown to be quite different in the presence of free carriers but, surprisingly, of similar strength. The differences are illustrated by the resonant structure of the $n = +1$ sideband. Instead of having several sharp excitonic resonances as in an equivalent undoped sample, there is only one broad resonance in the doped sample. The frequency of this resonance matches that of the independently measured intersubband plasmon, the

collective intersubband oscillation which couples to THz light. Thus sidebands at NIR frequencies can probe the coherent dynamics of electrons driven at much lower THz frequencies. The results are explained qualitatively in terms of a second order nonlinear susceptibility ($\chi^{(2)}$) model.

The samples consist of ten periods of double GaAs QWs, nominally 100 and 120 Å wide and separated by a 25 Å $\text{Al}_{0.2}\text{Ga}_{0.8}\text{As}$ tunnel barrier. The sample structure is displayed at the top of Fig. 1. Each pair of wells is separated by a 410 Å (920 Å) $\text{Al}_{0.3}\text{Ga}_{0.7}\text{As}$ barrier for the undoped (doped) sample. The difference between the widths of the GaAs wells breaks inversion symmetry in the growth direction, thus allowing the generation of $n = +1$ sidebands at zero bias. Furthermore, the tunnel-splitting produces a spacing between electron subbands in the range of our THz source, the University of California-Santa Barbara (UCSB) free electron laser. In the doped sample, there is silicon δ doping in the middle of the 920 Å barriers between each pair of coupled wells. This gives $\sim 1.2 \times 10^{11} e/\text{cm}^2$ per well, as determined by capacitance-voltage measurements. Some band bending in the vicinity of the doped double QWs is calculated due to space-charge fields, but the potentials and charge densities are nearly identical for each double QW except for the one closest to the surface. This active region is grown in-between two doped, 70 Å wide QWs. These QWs are contacted ohmically and used to apply a growth-direction electric field (E_{bias}) to the sample, tuning the ISB collective mode frequency [as measured by Fourier-transform infrared (FTIR) spectroscopy and plotted in the inset of Fig. 1(b)] and the optical properties. For most measurements the electric field was pulsed for less than 1 ms to avoid tunneling between wells. The active region and gate QWs are grown on a 30-period distributed Bragg reflector (DBR), designed to reflect the incident laser and the sidebands, which would otherwise be absorbed in the semi-insulating GaAs substrate. In order to maximize interaction with the NIR beam, the coupled wells in the doped sample are placed at the nodes produced by interference between the incident and reflected NIR beams.

The photoluminescence (PL) and reflectivity of the two

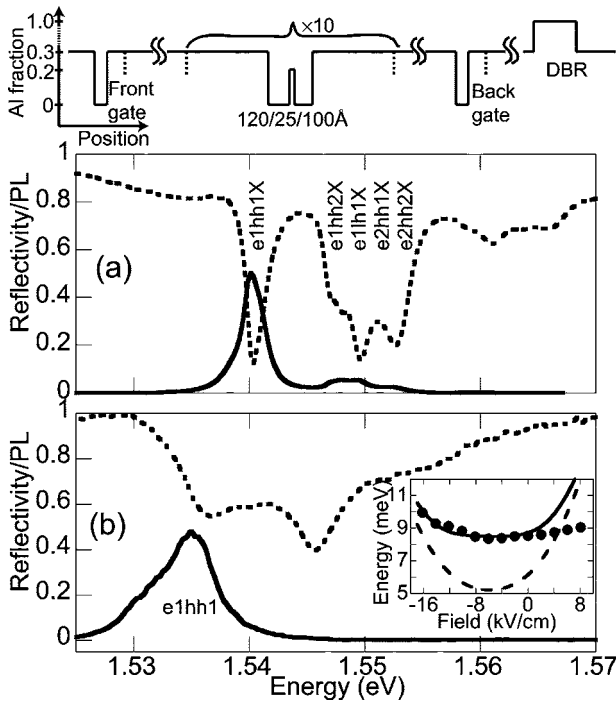


FIG. 1. PL (solid line) and reflectivity (dashed line) of the (a) undoped and (b) doped samples at zero bias taken at ~ 11 K. For PL, the samples were excited at 777 nm with an intensity of ~ 9 W/cm² for the undoped sample and ~ 30 W/cm² for the doped sample, and both were normalized to 0.5. The interband transitions in (a) are labeled according to theory, but the assignments are uncertain near 1.55 eV because several absorption lines overlap. The doped sample structure is displayed above (a). Doping is indicated by vertical dashed lines. In the undoped sample, the doping adjacent to the coupled quantum wells is absent. The inset in (b) plots the ISB absorption tuning as measured by FTIR (solid dots) along with the calculated dressed (solid line) and bare (dashed line) ISB frequencies. Band bending due to space-charge fields is included in the calculations.

samples are shown in Fig. 1, where the reflectivity is similar to a transmission measurement due to the DBR. In the undoped sample [Fig. 1(a)] there is sharp PL from the lowest state, $e1hh1X$, and a number of sharp, exciton absorption lines (labeled by theory).⁵ In the doped sample [Fig. 1(b)], the absorption is much broader as continuum absorption plays more of a role due to exciton screening.¹⁰ The onset of absorption, at ~ 1.534 eV, can be taken as the Fermi edge, which is near the peak of the PL. The width of the PL reflects the fact that electrons from the Fermi energy to the bottom of the conduction band (a width of ~ 4.2 meV based on the charge density) can recombine with holes. The obvious shift in PL between the doped and undoped samples may be due to band gap renormalization.¹¹

The geometry for sideband experiments is illustrated on the right side of Fig. 2. The sample was mounted in a closed-cycle He cryostat, where its temperature was kept constant between 10 and 16 K. The THz beam was coupled into the edge of the sample with its polarization perpendicular to the QW plane, allowing ISB transitions. The dielectric waveguide modes of the sample give in-plane electric fields and

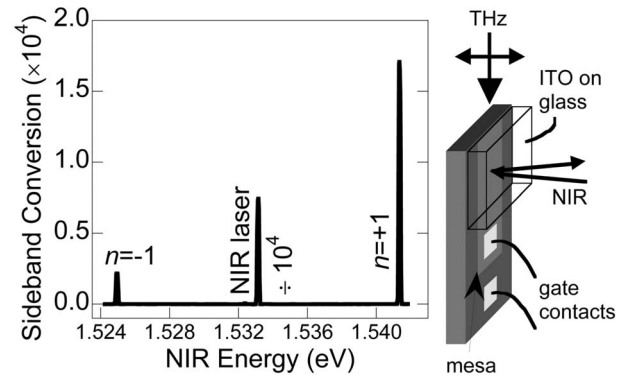


FIG. 2. Sideband spectrum taken at ~ 11 K with $\omega_{THz} = 2.0$ THz (8.2 meV) at ~ 730 kW/cm². The NIR laser signal is divided by $\sim 1 \times 10^4$. $E_{bias} = 5.8$ kV/cm. The experimental geometry is to the right of the figure.

substantially reduce the electric field at the surface. Glass coated with indium tin oxide (which conducts at THz frequencies) was pressed onto the sample frontside, improving the surface electric field while leaving the frontside transparent to NIR light. The THz beam was on for about 4 μ s at a repetition rate of 1.5 Hz with a maximum power of ~ 3 kW. It was focused onto the sample with an off-axis parabolic mirror ($f/2.4$) to a spot measured to be between 0.3 and 1.2 mm in diameter, for THz frequencies between 3.4 and 0.66 THz, respectively. Typically, the intensity was attenuated to ~ 40 kW/cm² (just outside the sample).

The NIR beam, which came from a cw tunable Ti:sapphire laser, was incident perpendicular to the sample and typically focused to an intensity of roughly 25 W/cm². It then made a double pass through the sample active region, by reflecting off the DBR, and was sent to a 0.85 m double monochromator, where it was detected by a photomultiplier tube.

Figure 2 displays a typical sideband spectrum for the

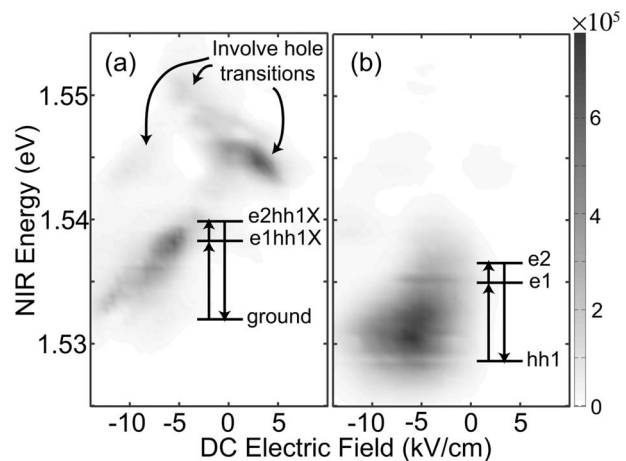


FIG. 3. The $n = +1$ sideband resonance maps of (a) the undoped and (b) doped samples at $\omega_{THz} = 2.0$ THz (8.2 meV), taken by varying ω_{NIR} and E_{bias} , while always measuring the $n = +1$ sideband. The sideband conversion for each point is represented on a grey scale, displayed on the right. The maps were taken at ~ 12 K with a THz intensity of ~ 18 kW/cm² and a NIR intensity of ~ 25 W/cm².

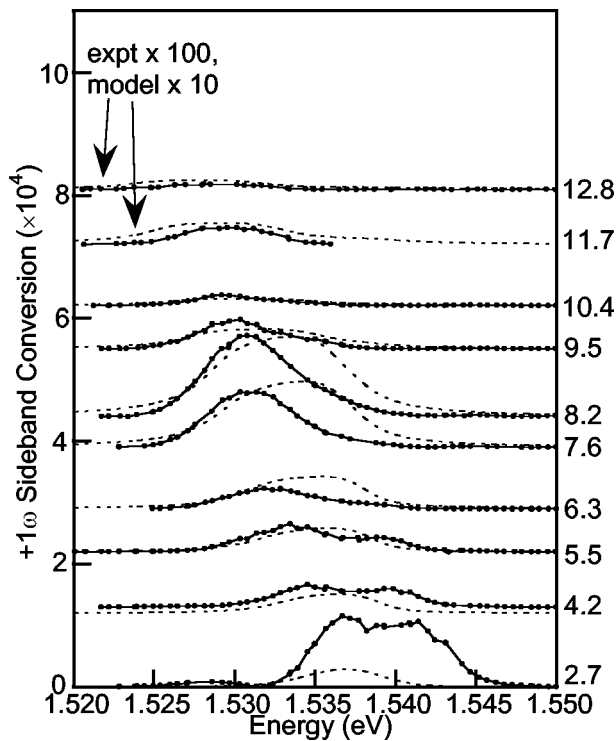


FIG. 4. The $n=+1$ sideband resonance spectra (solid dots and lines) of the doped sample taken with various THz frequencies, all with intensities near 40 kW/cm^2 . The temperature was between 11 and 16 K, and E_{bias} was at 5.8 kV/cm . Each point represents the sideband signal when ω_{NIR} is tuned to the value on the horizontal axis. The spectra are vertically offset and labeled according to ω_{THz} . $\chi^{(2)}$ model calculations (dashed lines) are plotted for comparison. Spectra at $\omega_{THz}=11.7$ and 12.8 meV are multiplied by 100 and their model curves are multiplied by 10 for clarity.

doped sample. The reflected NIR laser (attenuated by 10^4) is at 1.533 eV with $n=\pm 1$ sidebands offset by 8.2 meV , the THz frequency. The ratio of the $n=+1$ sideband power to the incident laser power, called the conversion efficiency, is measured to be $\sim 1.7 \times 10^{-4}$. This is the same order of magnitude conversion efficiency as in the undoped sample. Higher order sidebands were extremely small under these conditions.

Sideband generation is strongest when the NIR and THz frequencies (ω_{NIR} and ω_{THz}) are resonant with interband (IB) and ISB transitions, respectively. Figures 3(a) and 3(b) display $n=+1$ sideband resonance maps for the undoped and doped samples. These are obtained by scanning E_{bias} and ω_{NIR} while measuring the sideband. Scanning E_{bias} varies the ISB spacing, bringing it into resonance with ω_{THz} , while scanning ω_{NIR} brings it into resonance with IB transitions. There are several sharp excitonic resonances for the undoped sample, which have been studied previously and assigned to particular transitions.⁵ The lower-energy resonance only involves a change in electron state while the other resonances involve hole transitions. In the doped sample, only the resonance involving electron transitions remains significant. The resonance is much broader in NIR frequency as it involves continuum states instead of exciton states, and broader in E_{bias} as ISB tuning is screened somewhat by the electron gas.

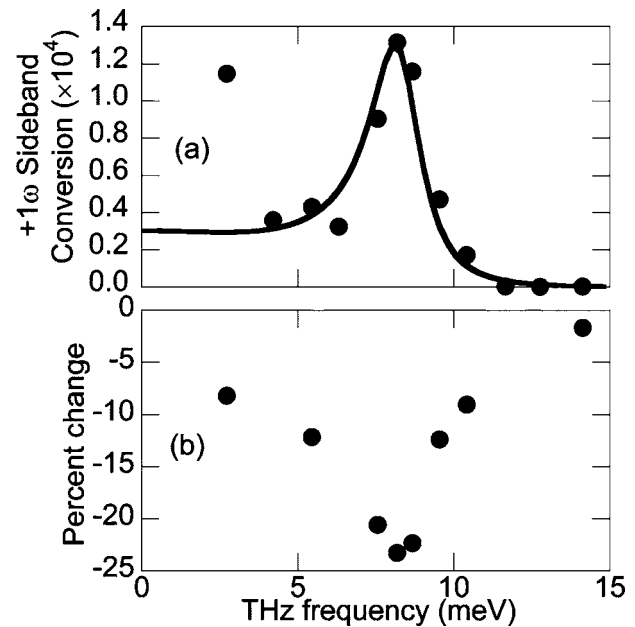


FIG. 5. (a) Peak values of the $n=+1$ sideband resonance spectra (solid dots) for the doped sample and the peak values of the $\chi^{(2)}$ model curves (solid line) plotted vs ω_{THz} . (b) Percent change in the integrated PL of the doped sample with the THz field on at an intensity of $\sim 40 \text{ kW/cm}^2$.

For the doped sample, the sideband intensity (on resonance) increased linearly with NIR intensity up to the highest NIR intensity available, $\sim 1500 \text{ W/cm}^2$. In the undoped sample saturation began at $\sim 160 \text{ W/cm}^2$. This difference likely occurred because the sideband resonance in the doped sample is just below the absorption edge, so few carriers were generated. Also, the addition of optically excited carriers in the doped well should have little effect since there is already significant charge density. As a function of THz intensity, both undoped and doped samples began to saturate at $\sim 80 \text{ kW/cm}^2$. This is surprising since resonant ISB absorption has been shown to start saturating at only $\sim 1 \text{ W/cm}^2$.¹²

Valuable information can be obtained by measuring the sideband signal as a function of ω_{THz} . Figure 4 displays the $n=+1$ sideband resonance scans at many different THz frequencies. These data were taken with $E_{bias} \sim 5.8 \text{ kV/cm}$, where the ISB absorption was measured to be at $\sim 8.3 \text{ meV}$ [see inset of Fig. 1(b)]. The resonance scan at 8.2 meV was closest to this frequency and had only a single resonance centered below the PL peak, despite the many IB resonances shown in Fig. 1. Resonance scans near 8.2 meV and at higher ω_{THz} had only one significant resonance that redshifted as ω_{THz} increased. For lower ω_{THz} , there were several resonances at higher ω_{NIR} . Figure 5(a) plots the peak of each sideband resonance scan as a function of ω_{THz} , showing the resonance at the ISB absorption frequency as well as a significant low frequency response. A similar behavior was seen in undoped square QWs but was due to purely IB processes.⁴

Sideband generation is a measure of the coherent response of the QW, but we have also probed the incoherent response by measuring the change in PL when the THz field is present. The electron gas is heated up by the THz beam, quenching the PL and shifting the Fermi distribution as seen

in similar systems.^{13,14} Figure 5(b) displays the percent change in the integrated PL as a function of the THz frequency. A single resonance near the ISB absorption is visible, as would be expected when the dominant heating mechanism is ISB absorption.

A qualitative understanding of THz-optical mixing in the doped sample can be obtained from a $\chi^{(2)}$ model. We will only consider three subbands: heavy hole 1 (*hh1*), electron 1

(*e1*), and electron 2 (*e2*). This approximation makes sense as the sideband resonance spectra with $\omega_{THz} > 5.5$ meV have one dominant resonance near the *e1-hh1* transition. This model has been applied to doped GaAs QWs previously.¹⁵ Taking an expression for $\chi^{(2)}$ from Ref. 16 and applying it to this system, the result after eliminating nonresonant and dipole forbidden terms is

$$\chi_{xx}^{(2)}(\omega_{NIR} + \omega_{THz}) \propto \mu_{1n}^x \mu_{nv}^z \mu_{v1}^x \sum_{n,\nu=2,3} \int_0^\infty k dk \frac{\rho_{11}(k) - \rho_{v\nu}(k)}{[E_{n1}(k) - \omega_{SB} - i\gamma_{n1}][E_{v1}(k) - \omega_{NIR} - i\gamma_{v1}]} - \frac{\rho_{v\nu}(k) - \rho_{nn}(k)}{[E_{n1}(k) - \omega_{SB} - i\gamma_{n1}][E_{n\nu}(k) - \omega_{THz} - i\gamma_{n\nu}]} \quad (1)$$

The indices 1, 2, and 3 represent the *hh1*, *e1*, and *e2* subbands, respectively, and k is the in-plane wave vector. $E_{lm}(k)$ is the energy of the l th subband minus the m th subband, both at wave vector k , and μ^x (μ^z) is an IB (ISB) dipole matrix element. $\rho_{mm}(k)$ is the equilibrium occupation function of the m th subband, and γ_{lm} represents the dephasing rate between subbands l and m .

The first term contains IB population differences and IB resonant denominators, and will be nonzero even without doping. A similar term was used in modelling sidebands in undoped QWs.⁴ When $n \neq \nu$, the first term is in resonance when ω_{NIR} and $\omega_{sideband}$ match up with IB transitions, giving an indirect ISB resonance. When $n = \nu$, the first term can only be in resonance for $\omega_{THz} < \gamma_{v1}$, and it only involves one IB matrix element and the asymmetry, $\mu_{v\nu}^z$. For these reasons, the $n = \nu$ first term is interpreted as resulting from the quasi-static modulation of the IB absorption, and gives rise to the low ω_{THz} sidebands. The second term in Eq. (1) requires an ISB population difference and has one ISB resonant denominator, so it represents sidebands due to ISB excitations. Near the ISB transition, this second term is significantly larger than the others for a Fermi energy of several milli-electronvolts, as in these experiments. Thus, as ω_{THz} is varied, there is an interplay between sidebands due to excitations of the electron gas, and those due to IB processes.

A complication when evaluating Eq. (1) is that the Coulomb interaction strongly modifies the potential well and the subband energies.¹⁷ The Schrödinger equation must be satisfied with Poisson's equation self-consistently in order to correctly include the Coulomb interaction. The ISB spacing (or bare ISB frequency) was calculated by such a self-consistent program as a function of the dc electric field and is plotted in the inset of Fig. 1(b).¹⁸ However, the Coulomb interaction also modifies the dynamics of the QW, such that a driving field induces collective excitations of the electron gas called "intersubband plasmons"¹⁷ ["charge density excitations" in the literature on Raman spectroscopy of two-dimensional electron gases (2DEGs)].¹⁹ The frequency of this collective excitation, called the dressed frequency, along with the measured absorption, is also plotted in the inset of Fig. 1(b). The disagreement between the two at positive voltages is not well understood.

A simple way to correct the $\chi^{(2)}$ model is to use the dressed frequency, 8.3 meV, for the ISB term while using the bare ISB frequency, ~ 5.2 meV, for the IB terms [see inset of Fig. 1(b)]. Using this correction, Eq. (1) was evaluated using dipole matrix elements calculated for an empty well and with $\gamma_{IB} = 2$ meV and $\gamma_{ISB} = 1$ meV, values which gave the best fit. The 2D band gap was also adjusted to fit the lower edge of the measured PL at 1.532 eV. The subband occupation function of *e1* was approximated as a step function while *hh1* and *e2* were treated as full and empty, respectively. The intensity of the $n = +1$ sideband is proportional to $|\chi^{(2)}|^2$, which is plotted next to the experimental data in Fig. 4. The maxima of $|\chi^{(2)}|^2$ are plotted as a function of ω_{THz} in Fig. 5(a).

The model accurately predicts the strong resonance near the dressed ISB frequency and the significant signal at low frequencies. It also predicts the redshift of the NIR resonance as ω_{THz} increases. However, the signal at $\omega_{THz} = 2.7$ meV is significantly stronger than predicted, and the signal above $\omega_{THz} = 10.4$ meV is much weaker than predicted. It may be that comparing the spectra with the same intensity outside the sample introduces this type of error as the intensity coupled to the QW layers may depend on the ω_{THz} . The extra resonances at low ω_{THz} are likely due to higher states similar to those in Fig. 3(a), which are not considered in the model. Finally, the widths and positions of the NIR resonances near $\omega_{THz} = 8.3$ meV are quite different from the model and cannot be improved by adjusting the γ 's. A challenge remains to fully explain the experimental results, perhaps using a theory which includes the electron-electron and electron-hole interactions *ab initio*.

THz-optical mixing has been measured for the first time in doped QWs, showing strikingly different resonant behavior than in undoped QWs. The most important distinction is that sidebands in doped QWs are primarily sensitive to the collective excitations of the electron gas, as demonstrated by the large resonance at the dressed ISB frequency. This fact allows the use of THz-optical mixing to probe ISB dynamics, providing a useful diagnostic for ISB devices such as THz quantum cascade lasers.²⁰ The THz fields in these devices are comparable to those used in these experiments.²¹ Using NIR light as opposed to FIR light has the advantage of being able

to probe very small areas, to use mature NIR optics, detectors, spectrometers, and to target specific QWs based on their IB transitions. These benefits are similar to those of Raman scattering,¹⁹ but sideband generation is uniquely suited to probe the *coherent* response of electrons to THz driving. Additionally, exciting effects have been predicted for doped QWs in strong THz fields, such as period-doubling bifurcations to chaos,²² which may be more easily observed using

THz-optical mixing. The $\chi^{(2)}$ model provides a good qualitative understanding of THz-optical mixing and reproduces many of the experimental trends.

We thank D. S. Citrin for useful discussions on this subject and acknowledge support from NSF Grant No. DMR 0244390 and Sun Microsystems.

*Present address: JILA, University of Colorado, Boulder, CO 80309, USA.

†Present address: V. Birkedal née Ciulin, Department of Chemistry, University of Aarhus, Langelandsgade 140, DK-8000 Aarhus C, Denmark.

‡Present address: Voxel, Inc., Beaverton, OR 97005, USA.

¹J. Shah, *Ultrafast Spectroscopy of Semiconductors and Semiconductor Nanostructures* (Springer, New York, 1996).

²J. Cerne, J. Kono, T. Inoshita, M. Sherwin, M. Sundaram, and A. C. Gossard, *Appl. Phys. Lett.* **70**, 3543 (1997).

³J. Kono, M. Y. Su, T. Inoshita, T. Noda, M. S. Sherwin, S. J. Allen, and H. Sakaki, *Phys. Rev. Lett.* **79**, 1758 (1997).

⁴V. Ciulin, S. G. Carter, M. S. Sherwin, A. Huntington, and L. A. Coldren, *Phys. Rev. B* **70**, 115312 (2004).

⁵M. Y. Su, S. G. Carter, M. S. Sherwin, A. Huntington, and L. A. Coldren, *Appl. Phys. Lett.* **81**, 1564 (2002).

⁶S. G. Carter, V. Ciulin, M. S. Sherwin, M. Hanson, A. Huntington, L. A. Coldren, and A. C. Gossard, *Appl. Phys. Lett.* **84**, 840 (2004).

⁷M. Y. Su, S. G. Carter, M. S. Sherwin, A. Huntington, and L. A. Coldren, *Phys. Rev. B* **67**, 125307 (2003).

⁸T. Inoshita and H. Sakaki, *Physica B* **249–251**, 534 (1998).

⁹A. V. Maslov and D. S. Citrin, *Phys. Rev. B* **62**, 16686 (2000).

¹⁰C. Delalande, J. Orgonasi, J. A. Brum, G. Bastard, M. Voos, G. Weimann, and W. Schlapp, *Appl. Phys. Lett.* **51**, 1346 (1987).

¹¹D. A. Kleinman and R. C. Miller, *Phys. Rev. B* **32**, 2266 (1985).

¹²K. Craig, B. Galdrikian, J. N. Heyman, A. G. Markelz, J. B. Williams, M. S. Sherwin, K. Campman, P. F. Hopkins, and A. C. Gossard, *Phys. Rev. Lett.* **76**, 2382 (1996).

¹³R. Romestain and C. Weisbuch, *Phys. Rev. Lett.* **45**, 2067 (1980).

¹⁴N. G. Asmar, J. Cerne, A. G. Markelz, E. G. Gwinn, M. S. Sherwin, K. L. Campman, and A. C. Gossard, *Appl. Phys. Lett.* **68**, 829 (1996).

¹⁵A. Neogi, Y. Takahashi, and H. Kawaguchi, *J. Opt. Soc. Am. B* **14**, 570 (1997).

¹⁶R. W. Boyd, *Nonlinear Optics* (Academic, San Diego, 1992), Chap. 3, p. 137.

¹⁷M. Helm, *Semicond. Semimetals* **62**, 1 (2000).

¹⁸In these calculations, the tunnel barrier was made 12% wider to better fit the experimental data. The $\text{Al}_{0.3}\text{Ga}_{0.7}\text{As}$ and $\text{Al}_{0.2}\text{Ga}_{0.8}\text{As}$ conduction band offsets were set as 300 and 200 meV, respectively.

¹⁹G. Abstreiter, R. Merlin, and A. Pinczuk, *IEEE J. Quantum Electron.* **QE-22**, 1771 (1986).

²⁰R. Kohler, A. Tredicucci, F. Beltram, H. E. Beere, E. H. Linfield, A. G. Davies, D. A. Ritchie, R. C. Iotti, and F. Rossi, *Nature (London)* **417**, 156 (2002).

²¹D. S. Citrin (private communication).

²²B. Galdrikian and B. Birnir, *Phys. Rev. Lett.* **76**, 3308 (1996).